

PRISM: A Framework Harnessing Unsupervised Visual Representations and Textual Prompts for Explainable MACE Survival Prediction from Cardiac Cine MRI

Haoyang Su^{†1,2,3}, Jin-Yi Xiang^{†4}, Shaohao Rui^{2,3,4}, Yifan Gao^{2,5}, Xingyu Chen⁴, Tingxuan Yin⁴, Xiaosong Wang^{*2,3}, and Lian-Ming Wu^{*4}

¹Fudan University, Shanghai, China

²Shanghai Innovation Institute, Shanghai, China

³Shanghai Artificial Intelligence Laboratory, Shanghai, China

⁴Shanghai Jiao Tong University, Shanghai, China

⁵School of Biomedical Engineering (Suzhou), Division of Life Science and Medicine, University of Science and Technology of China, Hefei, China

[†]These authors contribute equally to this work.

^{*}Corresponding authors

Abstract

Accurate prediction of major adverse cardiac events (MACE) remains a central challenge in cardiovascular prognosis. We present PRISM (Prompt-guided Representation Integration for Survival Modeling), a self-supervised framework that integrates visual representations from non-contrast cardiac cine magnetic resonance imaging with structured electronic health records (EHRs) for survival analysis. PRISM extracts temporally synchronized imaging features through motion-aware multi-view distillation and modulates them using medically informed textual prompts to enable fine-grained risk prediction. Across four independent clinical cohorts, PRISM consistently surpasses classical survival prediction models and state-of-the-art (SOTA) deep learning baselines under internal and external validation. Further clinical findings demonstrate that the combined imaging and EHR representations derived from PRISM provide valuable insights into cardiac risk across diverse cohorts. Three distinct imaging signatures associated with elevated MACE risk are uncovered, including lateral wall dyssynchrony, inferior wall hyperventilation, and anterior elevated focus during diastole. Prompt-guided attribution further identifies hypertension, diabetes, and smoking as dominant contributors among clinical and physiological EHR factors. The source code is available at <https://github.com/Hoyant-Su/PRISM>.

Keywords: Major adverse cardiac events, Non-contrast survival prediction, Motion-aware multi-view distillation, Prompt-guided medical analysis

1 Introduction

Major adverse cardiovascular events (MACE), encompassing outcomes such as cardiovascular death, myocardial infarction, and hospitalization for heart failure, remain a significant cause of morbidity and mortality globally [1–4]. As a composite endpoint, accurate prediction of MACE is essential for informing clinical decisions, optimizing patient outcomes, and capturing clinically significant deterioration, which correlates with long-term prognosis. This makes MACE prediction central to cardiovascular risk stratification [5, 6]. Consequently, many predictive approaches, such as AI-driven methods [4, 7–15], have become increasingly critical in MACE prediction in recent years.

Traditional approaches [16–18] often purely rely on manually curated features derived from electronic health records (EHRs), which, despite their accessibility, offer refined but limited physiological resolution and may fail to reflect the dynamic nature of cardiac function. Alternatively, methods based on histopathological images [17, 19–22], while providing high-resolution cellular information, are inherently static and dimensionally restricted, making them less suitable for capturing organ-level or temporal characteristics

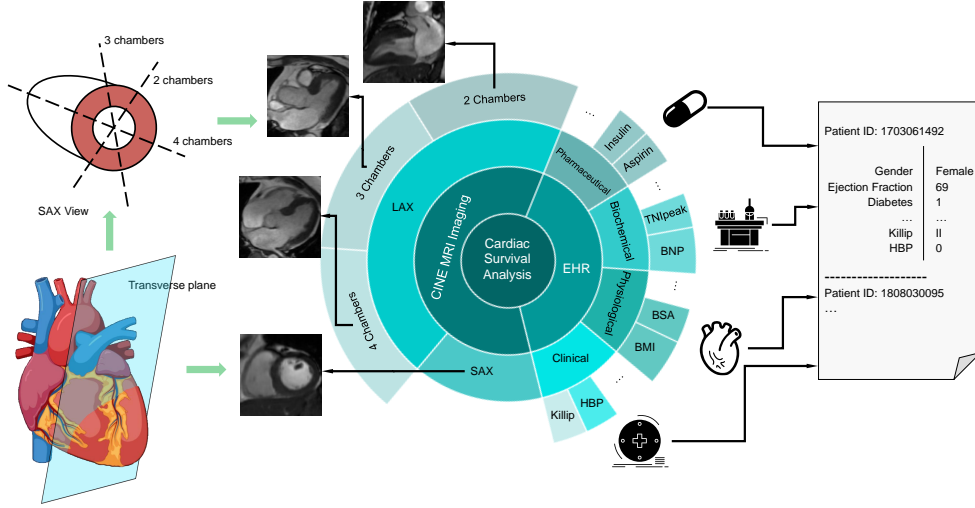


Figure 1: Overview of the cardiac survival analysis dataset featuring non-contrast cine MRI in short and long axis views and patient-level EHRs subcategorized into pharmaceutical, biochemical, physiological, and clinical domains.

relevant to adverse cardiovascular outcomes. These limitations hinder the extraction of comprehensive prognostic representations. In contrast, cardiac cine magnetic resonance imaging (MRI) provides organ-scale, high-resolution, and temporally dynamic information [23, 24], enabling the discovery of more expressive biomarkers associated with MACE [25–27]. In this context, as Fig. 1 shows, we exploit the complementary strengths of cine MRI and structured EHR data to construct a unified multimodal dataset tailored for integrative prognostic modeling.

Nevertheless, significant challenges remain. Contrast-enhanced acquisitions are often unavailable, and most medical images lack mask-level annotations, limiting the feasibility of expert-supervised modeling in real-world clinical settings. As a result, unsupervised paradigms become a prevailing approach in high-dimensional imaging representation learning [28–32]. However, unlike easily obtainable and superficial information contained in EHRs, conventional unsupervised image-to-image frameworks are confined to learning image-level representations, which, due to their inability to correlate with key attributes in EHRs, hinder the discovery of more granular biological biomarkers.

To address these limitations, we propose PRISM, a prompt-guided representation integration framework for survival modeling, which jointly learns spatiotemporal representations from cine MRIs and enables their interaction with structured EHR data, as illustrated in Fig. 2a. Image features are first extracted from cardiac cine sequences integrated with a multi-view distillation module, followed by alignment with EHR embeddings through a triangulation loss applied to the outputs of a student network. To further bridge the gap between image-derived features and downstream survival outcomes such as MACE, clinically meaningful prompts are incorporated to guide the model toward medically relevant semantics, thereby facilitating the discovery of prognostic imaging biomarkers indicative of cardiac risk. Building upon this, we derive clinically meaningful insights through the representations learned by PRISM by following the pipeline in Fig 2b. The image-derived features are utilized to reflect differential survival risk and MACE incidence. Building on these features, we introduce BiPromptSurv in Stage III as an outcome-guided analytical strategy that integrates semantically grouped EHR categories as anchors. By aligning model attention with domain-informed subgroups, this approach enables the identification of prognostically informative signatures and offers interpretable medical insights.

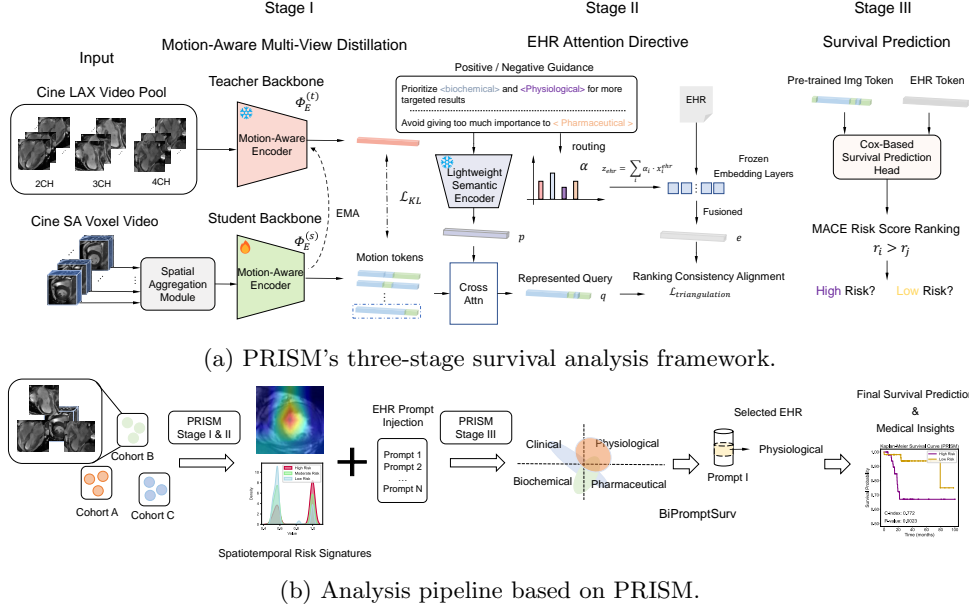


Figure 2: Details of the proposed framework and pipeline. (a): PRISM’s three-stage survival analysis framework. Multi-view cine MRI images passed through a teacher-student distillation network to obtain representation tokens enriched with spatiotemporal features, aligned hierarchically with EHR features under the influence of medically informed prompt aggregation. The refined image features are ultimately aggregated with EHR features in Stage III to yield survival analysis results. (b): Medical insights discovery pipeline based on PRISM. Deriving the association between spatiotemporal patterns of ventricular myocardium and MACE risk from the learned heatmap distributions, and exploring EHR features aiding in MACE assessment based on the BiPromptSurv strategy.

2 Results

2.1 Generalizability of PRISM across internal–external validation settings in multi-center cohorts

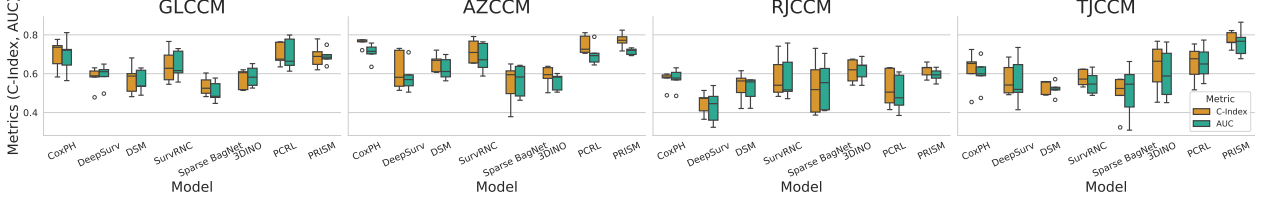
To rigorously evaluate the robustness and generalizability of our proposed framework, we conducted a comprehensive internal–external cross-validation (IECV) [33] analysis across four independent cohorts. PRISM was comparatively assessed against classical statistical models, neural network–based approaches, and contemporary state-of-the-art (SOTA) survival methodologies using the concordance index (C-index) and time-dependent area under the curve (AUC) as primary performance metrics. The comparator models encompassed the Cox proportional hazards model (CoxPH) [18], established as the clinical gold standard for survival analysis, as well as DeepSurv [17] and Deep Survival Machines (DSM) [16], designed to capture non-linear risk functions from tabular EHR data. Represented SOTA models in 3D medical imaging–based survival analysis, including Sparse BagNet and SurvRNC, were utilized to benchmark the performance of PRISM. Furthermore, to evaluate cross-paradigm efficacy within unsupervised representation learning, PRISM was benchmarked against two prominent self-supervised frameworks, namely PCRL [30] and 3DINO [28], which pretrained on large-scale, multimodal medical imaging datasets.

As illustrated in Fig. 3a and Fig. 3b, PRISM consistently demonstrated superior performance in survival analysis across both in-domain and out-of-domain validations, with its boxplot distributions exhibiting higher medians and narrower interquartile ranges compared to baseline models. This pattern was especially evident in the GLCCM and AZCCM cohorts, where alternative methods showed either lower central tendencies or pronounced variability across seeds. The stability of PRISM’s performance distributions indicates its robustness, thereby enhancing the trustworthiness of prognostic assessments and supporting more precise decision-making.

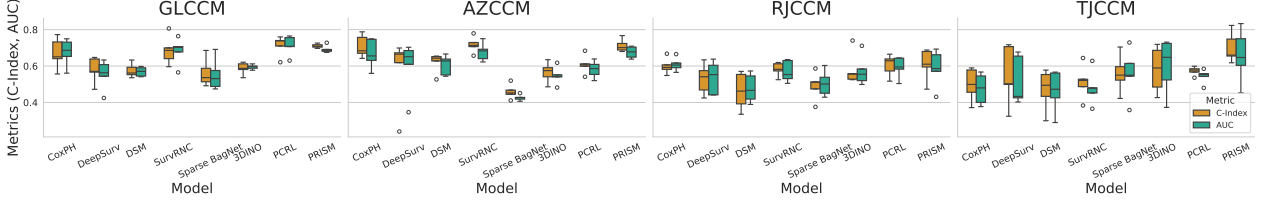
Compared to models rooted in clinical tabular modeling paradigms such as CoxPH, DeepSurv, and DSM, PRISM demonstrated marked gains particularly in scenarios characterized by multimodal feature heterogeneity, highlighting that image-driven alignment of latent EHR prognostic factors underpins its enhanced

effectiveness. While traditional models generally exhibited sharp performance decay in out-domain settings in the RJCCM and TJCCM cohorts, PRISM retained stable performance under distribution shift.

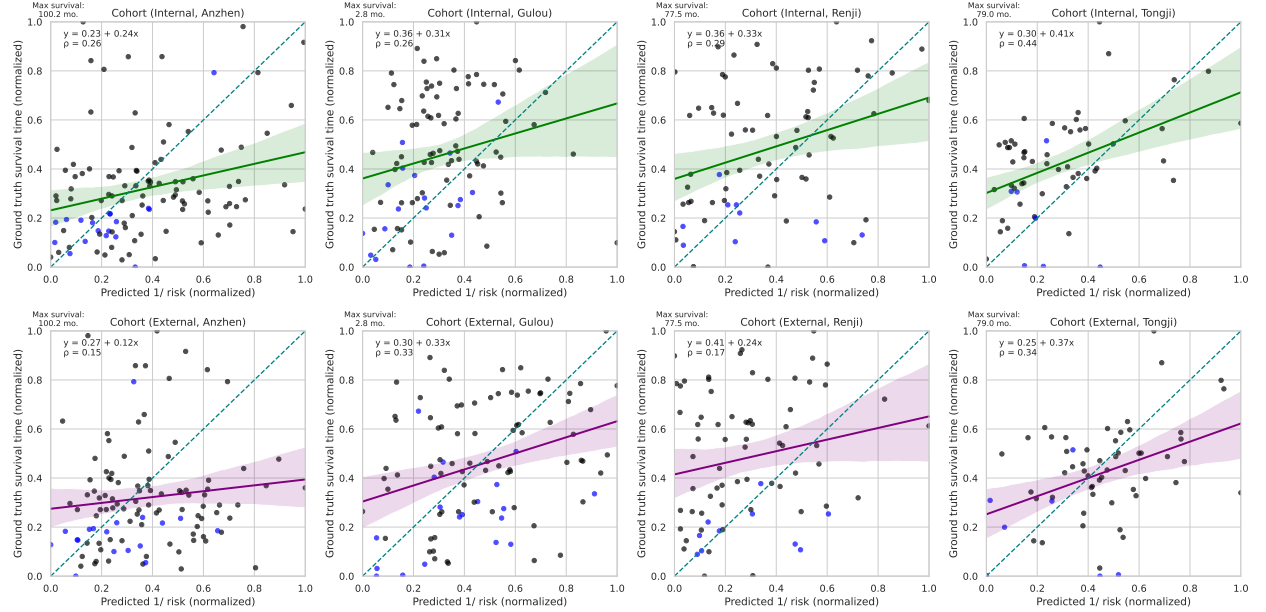
Furthermore, when benchmarked against advanced SSL frameworks pretrained on large-scale medical imaging corpora, including PCRL and 3DINO, PRISM consistently exhibited higher discriminative capacity across both low- and high-risk strata.



(a) Boxplots of C-index and AUC measured under in-domain conditions.



(b) Boxplots of C-index and AUC measured under out-domain conditions.



(c) Regression of predicted risk against ground-truth survival time.

Figure 3: Model survival analysis performance under the IECV setting. (a), (b): Boxplots of C-index (amber) and AUC (teal) across five data-splitting strategies under internal and external validation settings, respectively. (c): Regression analysis in the interval-external cross-validation setting, with model-predicted inverse risk (normalized) on the horizontal axis versus ground-truth survival time (normalized) on the vertical axis. Top panels represent internal validation and bottom panels show external validation in correlated cohorts. Cases with MACE=0 are denoted in black, while those with MACE=1 are indicated in blue.

Fig. 3c demonstrates the linear relationship between log-transformed inverse risk scores from our prognostic model and observed survival times in right-censored specimens. This further confirms the discriminative efficacy of computed risk in characterizing survival distributions. Specimens with MACE=1 consistently occupy high-risk positions across test sets in IECV setting. Critically, validation under external-center training conditions manifested only a minor slope reduction in average relative to internal validation. Specifically, the confidence band in the external GLCCM cohort exhibits progressive convergence with extended survival

times, yielding statistically narrower 95% confidence intervals versus the green internal band. This demonstrates time-invariant precision in survival estimation and temporal stability within the IECV experimental setting.

Corresponding to Fig. 3a and Fig. 3b, Table 1 and Table 2 present the detailed comparison results, including the ablation experiments. PRISM without Stage II represents an ablation version of our proposed model in which the visual features from Stage I are directly fed into survival analysis. The best and second-best performances for each cohort are highlighted in bold and underlined, respectively. It can be observed that PRISM demonstrates the highest average performance across the four cohorts, ranking first or second in most, and remaining highly competitive throughout. To further evaluate the significance of these results across random seeds, we combined the p -values obtained from each seed using Fisher’s method [34]. The test statistic was computed as $X^2 = -2 \sum_{i=1}^k \ln(p_i)$, which follows a χ^2 distribution with $2k$ degrees of freedom.

Table 1: Performance comparison (C-index) of different models across cohorts under IECV settings.

Model	GLCCM	AZCCM	RJCCM	TJCCM
Internal				
CoxPH	<u>0.698</u> ±0.071	<u>0.760</u> ±0.020	0.568±0.040	0.619±0.091
DSM	0.572±0.079	0.656±0.048	0.536±0.076	0.532±0.037
DeepSurv	0.553±0.095	0.616±0.092	0.545±0.104	0.593±0.087
SurvRNC	0.641±0.091	0.716±0.063	0.583±0.109	0.579±0.043
Sparse BagNet	0.536±0.050	0.547±0.110	0.532±0.146	0.495±0.102
3DINO	0.573±0.047	0.588±0.049	0.614±0.055	0.634±0.115
PCRL	0.701 ±0.052	0.749±0.044	0.526±0.089	0.649±0.098
PRISM (Ours, w/o Stage II)	0.600±0.031	0.671±0.049	<u>0.615</u> ±0.072	<u>0.730</u> ±0.079
PRISM (Ours)	0.690±0.055	0.772 ±0.035	0.617 ±0.033	0.775 ±0.037
External				
CoxPH	0.708±0.055	0.671±0.076	0.599±0.039	0.499±0.081
DSM	0.575±0.038	0.621±0.054	0.463±0.101	0.472±0.111
DeepSurv	0.559±0.125	0.579±0.171	0.553±0.139	0.565±0.160
SurvRNC	0.686±0.079	0.717 ±0.044	0.582±0.038	0.513±0.093
Sparse BagNet	0.563±0.077	0.459±0.040	0.492±0.077	0.559±0.103
3DINO	0.587±0.030	0.566±0.050	0.581±0.080	0.581±0.120
PCRL	0.714 ±0.049	0.609±0.046	0.605±0.053	0.573±0.021
PRISM (Ours, w/o Stage II)	0.617±0.061	0.679±0.047	0.665 ±0.088	<u>0.608</u> ±0.115
PRISM (Ours)	<u>0.710</u> ±0.010	<u>0.712</u> ±0.031	<u>0.609</u> ±0.077	0.701 ±0.075

As illustrated in Fig. 4, Kaplan–Meier survival curves [35] are presented for our proposed models, the clinical gold-standard CoxPH, and the strongest-performing comparative model PCRL under out-of-domain evaluation settings. The purple and yellow curves represent the high- and low-risk populations, respectively, stratified by the median of the model-predicted risk scores.

Examining the horizontal axis, due to the recency of data collection and limited follow-up windows, the GLCCM cohort exhibits relatively short survival durations within three months. This compressed time span leads to more confident p -values across models. As the survival time extends in other cohorts, the uncertainty in MACE risk prediction increases, as reflected by an increase in the p -value. This is also reflected by the flattening or overlapping of the high-risk survival curves in certain circumstances, such as PCRL on TJCCM. In contrast, PRISM consistently yields the smallest p -values across cohorts, while the average p -value of PRISM is approximately 16.19 times smaller than that of PCRL under the same target test set, indicating a much higher level of confidence to performance degradation over extended follow-up periods.

Table 2: Performance comparison (AUC) of different models across cohorts under IECV settings.

Model	GLCCM	AZCCM	RJCCM	TJCCM
Internal				
CoxPH	<u>0.693</u> \pm 0.083	<u>0.709</u> \pm 0.042	0.574 \pm 0.049	0.601 \pm 0.074
DSM	0.562 \pm 0.060	0.626 \pm 0.058	0.520 \pm 0.065	0.521 \pm 0.038
DeepSurv	0.543 \pm 0.105	0.583 \pm 0.070	0.526 \pm 0.112	0.574 \pm 0.095
SurvRNC	0.645 \pm 0.075	0.682 \pm 0.077	0.583 \pm 0.121	0.552 \pm 0.061
Sparse BagNet	0.507 \pm 0.054	0.562 \pm 0.084	0.542 \pm 0.130	0.509 \pm 0.140
3DINO	0.586 \pm 0.049	0.558 \pm 0.039	0.620 \pm 0.052	0.600 \pm 0.119
PCRL	0.699 \pm 0.075	0.699 \pm 0.051	0.500 \pm 0.087	0.657 \pm 0.092
PRISM (Ours, w/o Stage II)	0.606 \pm 0.052	0.667 \pm 0.055	0.592 \pm 0.068	<u>0.744</u> \pm 0.081
PRISM (Ours)	0.689 \pm 0.036	0.714 \pm 0.016	<u>0.593</u> \pm 0.030	0.760 \pm 0.066
External				
CoxPH	0.669 \pm 0.072	<u>0.676</u> \pm 0.067	<u>0.609</u> \pm 0.033	0.474 \pm 0.076
DSM	0.569 \pm 0.026	0.606 \pm 0.055	0.479 \pm 0.079	0.463 \pm 0.114
DeepSurv	0.552 \pm 0.108	0.599 \pm 0.130	0.551 \pm 0.118	0.559 \pm 0.132
SurvRNC	0.683 \pm 0.073	0.678 \pm 0.050	0.571 \pm 0.059	0.481 \pm 0.095
Sparse BagNet	0.552 \pm 0.087	0.426 \pm 0.016	0.505 \pm 0.070	0.559 \pm 0.135
3DINO	0.595 \pm 0.012	0.547 \pm 0.043	0.574 \pm 0.075	<u>0.600</u> \pm 0.145
PCRL	0.713 \pm 0.048	0.582 \pm 0.042	0.594 \pm 0.051	0.544 \pm 0.035
PRISM (Ours, w/o Stage II)	0.622 \pm 0.057	0.651 \pm 0.059	0.663 \pm 0.092	0.568 \pm 0.148
PRISM (Ours)	<u>0.692</u> \pm 0.019	<u>0.676</u> \pm 0.028	0.589 \pm 0.091	0.657 \pm 0.130

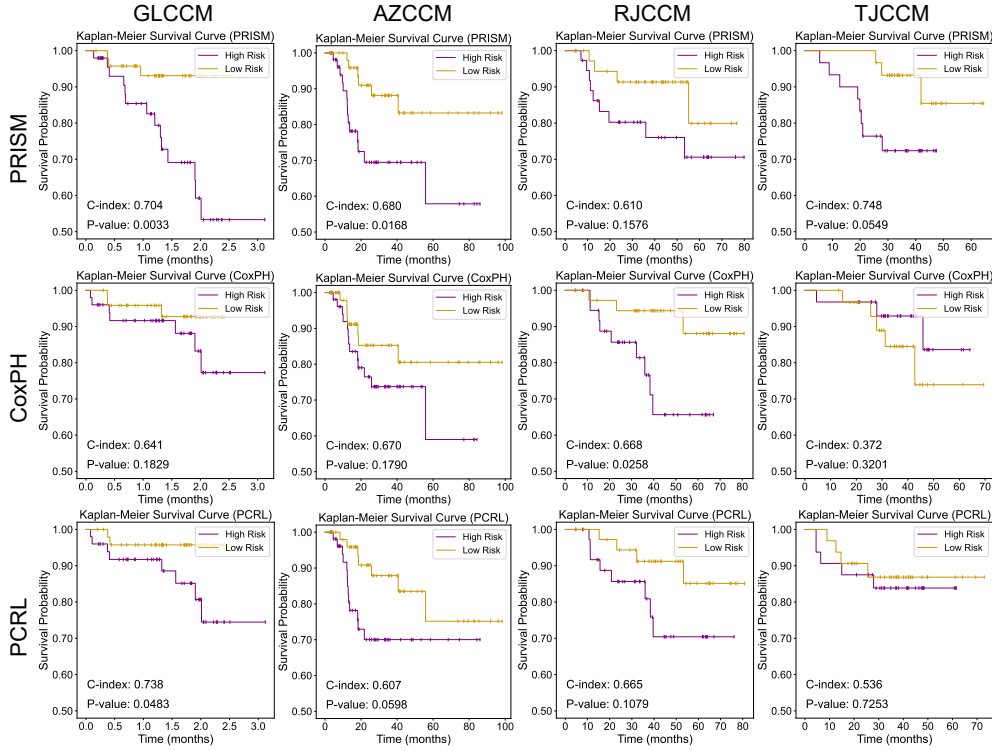
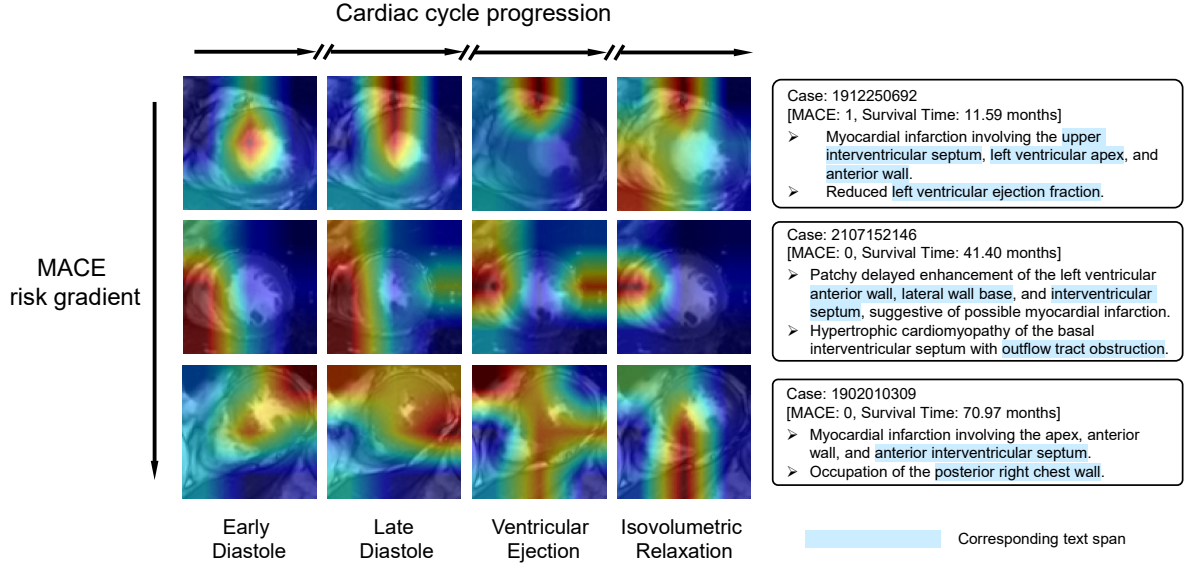
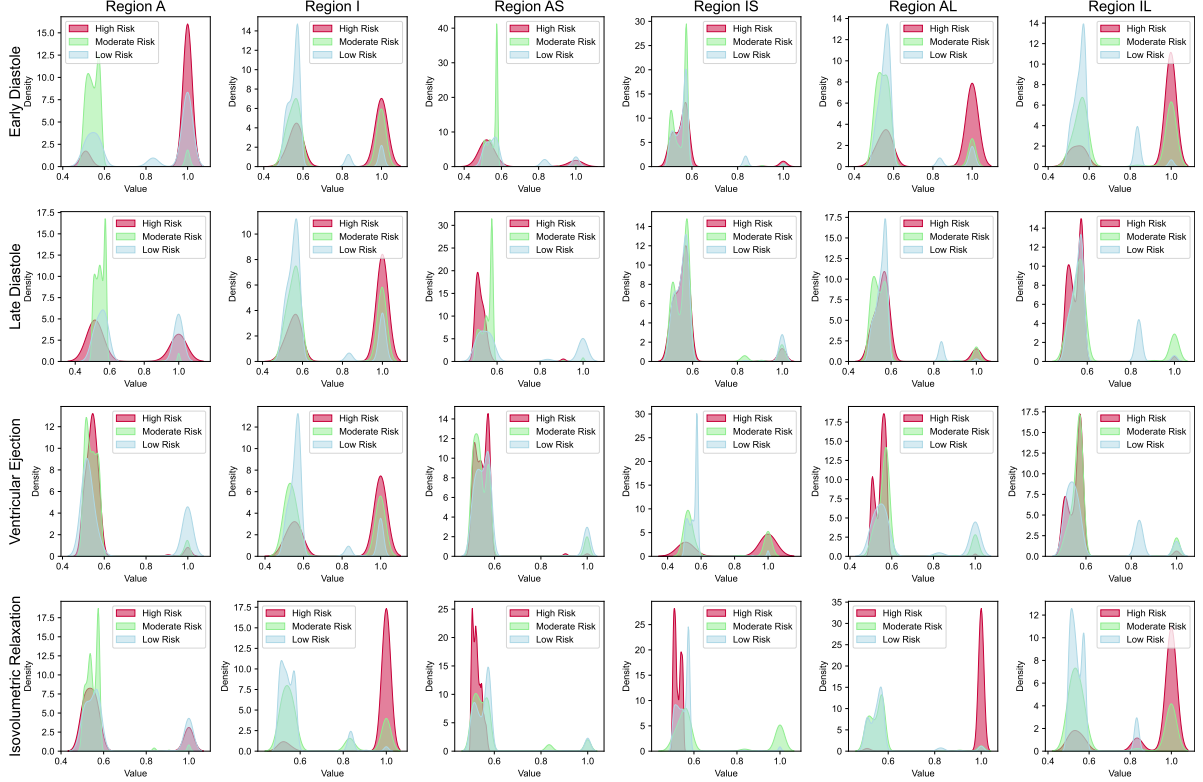


Figure 4: Kaplan-Meier survival plots across four cohorts (GLCCM, AZCCM, RJCCM, TJCCM) and three modeling strategies (PRISM, CoxPH, PCRL). p -value is incorporated as a metric to assess the statistical significance and reliability.



(a) Attention rollout of image tokens in Stage II across cardiac cycle phases.



(b) Spatiotemporal KDEs of predicted heatmap distributions in the SAX view.

Figure 5: Model attention and heatmap analysis across cardiac cycle phases and MACE risk. (a): Attention rollout of image tokens under stage II with horizontal axis representing typical cardiac cycle phases (early diastole, late diastole, ventricular ejection, isovolumetric relaxation) and vertical axis indicating increasing MACE risk levels. Text spans highlighted in light blue showing strong concordance between model attention and radiological diagnosis. (b), Spatiotemporally separated kernel density estimates of model-predicted heatmap distributions across three risk levels, six myocardial segments (A, I, AS, IS, AL, IL), and four cardiac cycle periods (early diastole, late diastole, ventricular ejection, isovolumetric relaxation), in the SAX view.

2.2 Visual signatures of MACE in cardiac motility

As Fig. 5a shows, with attention rollout applied during early diastole, late diastole, ventricular ejection, and isovolumetric relaxation, cross-attention distribution between the image-derived features and a medically guided prompt directing analytical capacity toward physiological aspects was visualized, revealing distinct phase-specific patterns of myocardial focus that corresponded to radiologically recognized regions of diagnostic relevance.

Radiological diagnostic reports established by board-certified physicians were served as reference standards for attention rollout validation. These expert-annotated reports were rigorously excluded from model training data throughout the unsupervised learning phase. For the subfigures, the spatial correspondence between cardiac anatomy and highlighted attention regions shows broad consistency with the described canonical structures, such as the four myocardial walls.

While the right ventricle itself was not directly implicated in the reported infarction, the attention pattern with extensive coverage over the right ventricular region in the upper subfigure may reflect secondary spatial proximity or structural interplay between the right heart border and adjacent thoracic pathology. This observation suggests that the model may possess the capacity to flag clinically relevant extracardiac abnormalities through contextual feature attribution.

On the other hand, representing a high-risk case with MACE and significantly reduced survival, the lower subfigure demonstrates progressive spatial redistribution of model attention. Following diastole, attention migrates from the left ventricle toward the anterior wall, subsequently returning to the left ventricular region post-systole and ejection, with eventual propagation toward the interventricular septum. This spatiotemporal trajectory aligns with diagnostic evidence of anterior wall myocardial infarction and reflects the model’s sensitivity to dynamically coupled biomarkers such as ejection fraction variations.

Spatiotemporal characterization of myocardial attention patterns in Fig. 5b reveals distinct risk-dependent signatures across cardiac phases and ventricular segments. The standard mid-ventricular segmentation scheme [36] was applied, dividing the left ventricular myocardium into six circumferential wall segments. Kernel density estimation [37] of normalized heatmap values demonstrates consistently localized attentional foci, with transitional intervals exhibiting markedly sparse distributions. This indicates pronounced gradient steepness rather than diffuse activation, reflecting the model’s capacity for targeted anatomical discrimination. In lateral segments (AL, IL), high-risk specimens exhibit significant phase-dependent redistribution. Diastolic phases display intensified focus relative to systolic attenuation, suggesting impaired relaxation-contraction coupling as a pathophysiological marker. Conversely, the inferior wall (segment I) manifests persistent hyper-attention across all phases in high-risk specimens, establishing this territory as a critical discriminator of adverse outcomes.

Septal regions (AS, IS) demonstrate functional homogeneity, with unimodal distributions centered near neutral values irrespective of risk stratification. This absence of differential engagement indicates limited pathological specificity in septal mechanics. The anterior wall (segment A) exhibits divergent risk-specific signatures, with moderate-risk specimens concentrating in low-attention zones while high-risk counterparts show early diastolic predominance.

Collectively, these signatures delineate three cardinal risk indicators, including lateral dyssynchrony, inferior hypersensitivity, and anterior diastolic elevated focus. The phase-dependent redistribution of attentional focus within lateral segments among high-risk subjects corresponds to established evidence positioning lateral strain delay as a superior marker of pathological left ventricular dyssynchrony [38]. Concordant with our findings, anterior diastolic elevated focus substantiates prior observations of the anterior wall’s pronounced vulnerability to diastolic impairment, particularly within metabolically compromised substrates, as documented in type 2 diabetes cardiomyopathy models [39]. Similarly, the inferior hypersensitivity identified in our computational framework recapitulates the predilection for inferior wall involvement in ischemic pathology, a territorially critical determinant of cardiac prognosis [40], thereby underscoring its pathognomonic role in myocardial ischemia-infarction continua.

2.3 BiPromptSurv-driven EHR analysis

Intuitively, comprehensive EHR integration yields the most accurate MACE risk stratification. However, our BiPromptSurv framework empirically identifies cohort-preferred EHR feature groups, enabling prompt-guided secondary survival analysis. By isolating salient feature subsets, this approach improves risk stratification consistency under controlled conditions, underscoring the prognostic value of selective feature integration. We introduced a set of syntactically diverse prompts absent from the model’s pre-training corpus. The

prompts were synthesized via DeepSeek-R1 70B [41], generating a prompt distribution, which extrapolated novel yet semantically aligned instructions from a small set of handcrafted exemplars. A lightweight routing module assigns these prompts to categorized EHR class weights.

Among the generated prompts, a handful exhibited consistent improvements in risk stratification fidelity across target cohorts under the BiPromptSurv framework’s instruction for secondary survival analysis. Notably, as illustrated in Fig. 6a, prompting with statements that focus on a single EHR category, such as **Design your metrics pipeline around <clinical>**, and using only 13 clinical-related features leads to a 1.2% increase in the mean AUC for the RJCCM cohort, albeit at the cost of higher cross-seed variance. Similarly, applying prompts like **Incorporate multimodal indicators from <clinical> and <physiological> information to enhance the precision of the machine learning model** led to improved survival prediction in both GLCCM and RJCCM cohorts by leveraging clinical and physiological features, outperforming models trained on the full feature set.

Building on this foundation, CoxPH model was employed, which serves as the gold standard and as the survival head within our framework, to conduct cohort-specific attribution analysis on the selected feature groups. Aggregated SHAP values were derived to demonstrate the contributions of different types of EHR features. As illustrated in Fig. 6b, CoxPH attribution reveals that clinical and physiological features dominate the EHR contribution in RJCCM and GLCCM cohorts, accounting for approximately 82.4% and 69.9% of the total SHAP values, respectively. This concordance confirms BiPromptSurv’s targeted feature selection efficacy while underscoring the interpretability of prompt-guided imaging features.

Furthermore, SHAP analysis was employed for fine-grained attribution, aiming to uncover how our model’s Stage II and III behaviors vary across different prompts and the respective contributions of specific categorized EHR features to survival analysis. Using PRISM, we identified and presented the top 10 most important features at the cohort level, among which is an `Aggregated_Img_feature` aggregated from the five core imaging features. Concordance was observed in GLCCM, where physiological indicators such as heart rate (HR), stroke volume (SV), and ejection fraction (EF), which are closely related to myocardial function, were included. This is consistent with the role of PRISM in extracting imaging features during Stage I. Meanwhile, clinical features such as hypertension, diabetes, and dyslipidemia also remained dominant. The same trend was observed in RJCCM, where physiological and clinical features accounted for 80% of the top 10. Additionally, the role of aggregated image features as the top-ranked primary contributors in the TJCCM cohort is prominently demonstrated in Fig. 3, further validating the effectiveness of the PRISM model in image analysis by achieving significant improvements over classical EHR models, SOTA methods, and unsupervised comparative approaches.

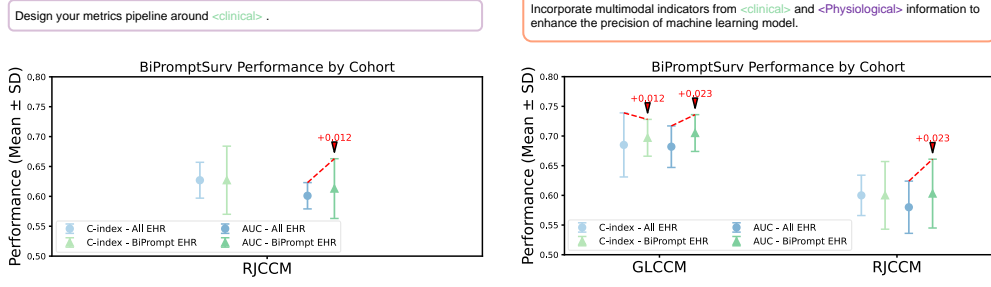
2.4 Individualized PRISM-based risk interpretation

A case study was conducted to illustrate PRISM risk estimates for event occurrence at successive time points within the same cohort, comparing representative MACE-positive patients with the mean profile of MACE-negative patients. As Fig. 7 shows, physician-curated EHR features supported the analysis and interpretation of these cases, elucidating their complication profiles and salient clinical characteristics.

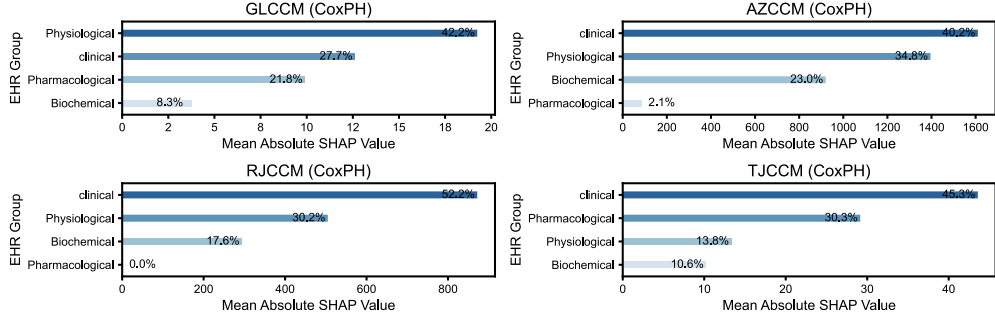
Case A and case B demonstrate PRISM’s risk predictions over approximately one year in typical high-risk cases. A more pronounced divergence in the risk curves is observed in case A, where PRISM’s risk prediction reached a significantly elevated level as early as 20 months post-prognosis. This can be partly attributed to the distinct quantitative differences in ventricular motion characteristics, such as markedly elevated end-systolic volume (ESV) and end-diastolic volume (EDV), coupled with a notably reduced EF. From the 25-frame multi-view imaging series, we selected the 1st, 11th, and 21st frames for analysis. Both SAX and LAX views reveal significantly enlarged ventricular volumes with minimal chamber variation throughout the cardiac cycle, corroborating the imaging-based evidence of severely impaired EF.

In contrast, among the listed complications strongly associated with MACE, case B exhibited two conditions, including microcirculatory disorder and ventricular aneurysm. Compared to MACE=0 samples, its differential EHR feature ranking showed less pronounced divergence than in case A, as reflected in the smaller Z-score deviation from zero. This observation may partly explain why PRISM adopted a more conservative approach in predicting MACE for case B.

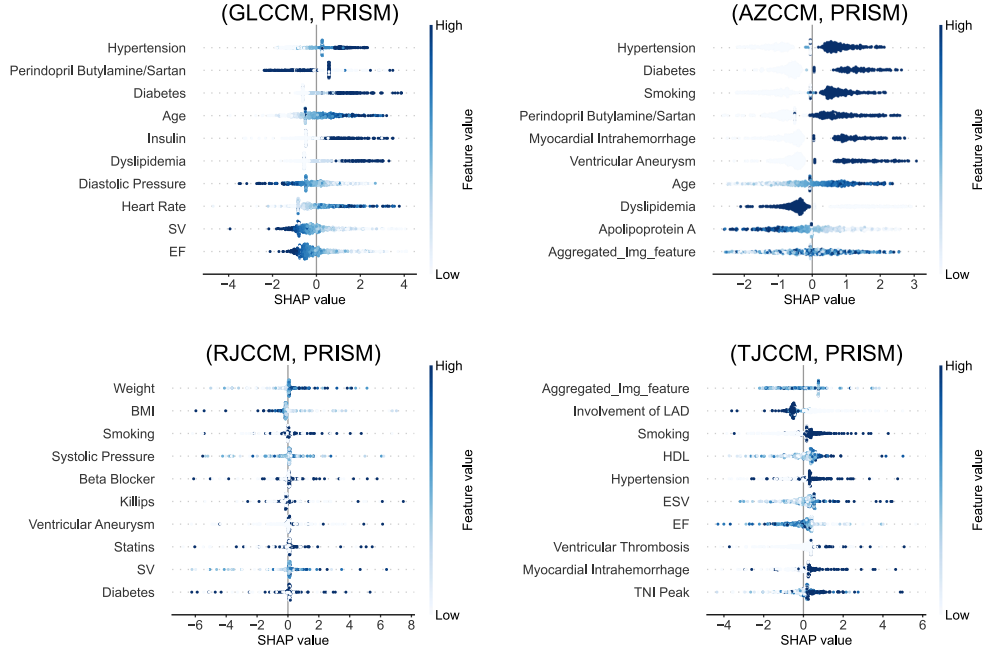
Case C represents the most misleading scenario in our study, specifically selected to demonstrate the model’s potential for prediction errors. This patient experienced a recurrent heart failure leading to MACE after 78 months of follow-up, despite displaying no high-risk indicators during initial assessment. Notably, baseline characteristics including age and apolipoprotein A levels were more favorable than those observed



(a) Performance gains with BiPromptSurv pipeline and comparison with all-EHR baseline.



(b) CoxPH-based cluster attribution of EHR categories for survival impact.



(c) SHAP attribution of PRISM highlighting top-ranked EHR and image features.

Figure 6: Statistical analysis results based on PRISM Stage II and Stage III. (a): Examples of prompts exhibiting performance improvement under the BiPromptSurv pipeline along with result comparisons. Dot plots with error bars in light blue and light green across five seeds are displayed. Red arrows indicate the increase in mean corresponding metrics compared to the all EHR setting. (b): Cluster attribution analysis based on CoxPH, showing contributions of each EHR category reflecting their survival analysis impact within the cohort. (c): Fine-grained SHAP attribution analysis of PRISM. Top-10 ranked features are presented along with top-5 image features aggregated as Aggregated_Img_feature.

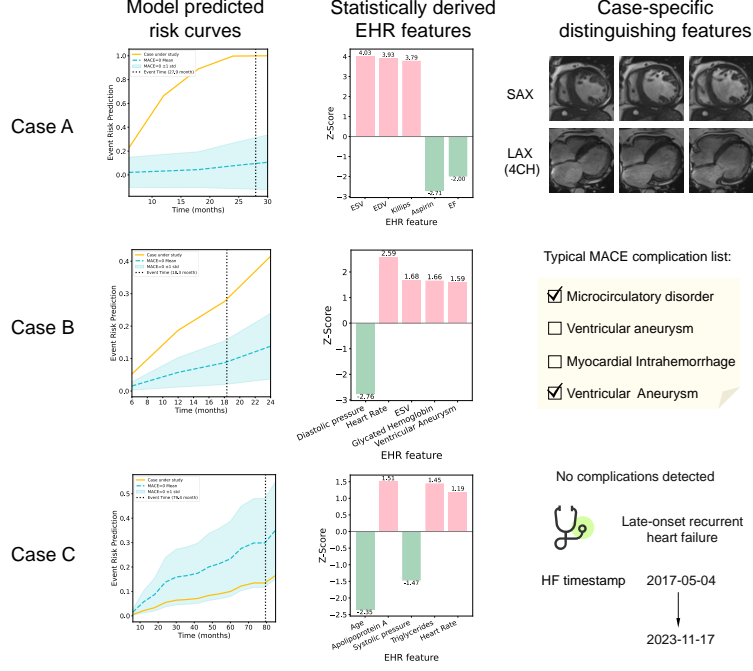


Figure 7: Case-specific risk profiling using PRISM. A teal color and an amber color are used to illustrate the temporal risk prediction trends of PRISM for the case under study and a MACE=0 sample from the same cohort, respectively. Statistically derived EHR features and case-specific distinguishing features are listed to highlight key evidence associated with the sample’s survival analysis.

in typical cases. This discordance between model predictions and actual outcomes emphasizes the critical importance of extended clinical surveillance, as early prognostic assessments may fail to identify delayed adverse events.

3 Discussion

A key finding of our study is the striking concordance between the spatiotemporal risk signatures identified by PRISM and established coronary artery territories. It is crucial to emphasize that this alignment emerged de novo from the model’s unsupervised learning process, without any prior anatomical or physiological knowledge of vascular distribution being encoded. This convergence is particularly significant given that myocardial infarction, a prototypical coronary artery disease, underlies the pathology of our study cohort. Specifically, the inferior hypersensitivity signature likely reflects residual dysfunction within the territory supplied by the right coronary artery, while the dynamic patterns of lateral dyssynchrony and anterior diastolic elevated focus correspond to regions perfused by the left anterior descending and circumflex arteries, respectively. This data-driven recapitulation of fundamental clinical pathophysiology serves as a tool capable of generating new hypotheses about how specific patterns of regional myocardial dysfunction contribute to the overall prognosis following an acute ischemic event, which elevates the clinical potential of our approach beyond simple risk stratification.

Integrating the cross-cohort SHAP value analyses derived from our PRISM model, we identified that among routinely obtained clinical assessments in standard hospital settings, hypertension and diabetes emerge as prominent potential biomarkers with high priority for predicting MACE. Notably, these comorbidities consistently ranked within the top 10 salient features across three of our independent centers. This finding underscores the persistent and critical role of traditional EHR variables alongside the advanced, unsupervised, image-based feature extraction facilitated by PRISM in survival analyses.

This finding has been corroborated in medical studies focused on EHR-based data mining. For instance, [42, 43] identified these three factors as having odds ratios substantially deviating from 1 among a wide range of EHR-derived features. Some studies[44, 45] directly targeted patient populations with the corresponding conditions to investigate cardiovascular risk. However, such studies are predominantly based on aggregated

clinical statistics, and few have initiated the investigation from high-dimensional medical imaging before incorporating multimodal clinical features. On the other hand, while EHR data contribute substantially to predictive performance, their center-specific nature raises important concerns regarding generalizability. Certain EHR-derived predictors previously established as pivotal for MACE prognostication, such as door-to-balloon (D2B) time [46], which may exhibit limited external validity due to inter-institutional variability and data scarcity. This heterogeneity accentuates the imperative for robust image-derived biomarkers and the refinement of methodologies for their extraction and integration, as these features potentially offer more scalable and universally applicable risk indicators. Ultimately, our findings advocate for a hybrid modeling paradigm that synergizes comprehensive EHR information with advanced imaging analytics to achieve optimal, generalizable cardiovascular risk assessment.

In addition to the population-level findings, the case study indicated that patients who experienced MACE frequently presented with complications such as microcirculatory disorder and ventricular thrombosis. Although these conditions may represent intermediate stages in the development of MACE, they do not constitute decisive determinants of the event itself.

4 Methods

4.1 Study Population and Inclusion Criteria

A total of 1970 patients were retrospectively analyzed from four tertiary medical centers in this study. Eligibility required confirmation of first-onset ST-segment elevation myocardial infarction through characteristic ischemic symptoms accompanied by significant ST-segment elevation (> 0.1 mV in limb leads or > 0.2 mV in precordial leads) in at least two contiguous leads. All enrolled cases received primary percutaneous coronary intervention within 12 hours of symptom onset and subsequently underwent cardiovascular magnetic resonance examination within 7 days following reperfusion. Exclusion criteria comprised previous myocardial infarction, contraindications to cardiovascular magnetic resonance, suboptimal imaging quality, or established non-ischemic cardiomyopathy diagnoses.

4.2 Follow-up Protocol and Endpoint Assessment

Patient follow-up commenced upon discharge following the index event and continued through December 31, 2024. Outcome data were systematically obtained through structured telephone interviews, standardized questionnaires, and scheduled clinical evaluations conducted at three-month intervals.

The primary composite endpoint of MACE incorporated four components: (1) mortality from any cause, (2) recurrent myocardial infarction as per the Fourth Universal Definition of Myocardial Infarction (2018), (3) unscheduled revascularization procedures, and (4) hospital admissions due to heart failure.

Heart failure diagnoses required either: (a) expert clinical confirmation or (b) documentation of new-onset symptomatic fluid retention necessitating diuretic therapy in patients demonstrating either left ventricular ejection fraction below 50% or elevated natriuretic peptide levels. Revascularization procedures were classified as unplanned if they were neither part of the initial therapeutic strategy nor scheduled to occur within 60 days post-index procedure.

All events occurring prior to cardiovascular magnetic resonance imaging were excluded from final analysis. An independent central laboratory conducted blinded adjudication of all reported clinical endpoints to ensure standardized event classification.

4.3 Image preprocessing: ventricular motion focus

Cardiac cine MRI sequences underwent mask-free motion analysis to quantify ventricular dynamics without contrast agents. Full cardiac volumes $\mathcal{V}^{(total)}$ were processed through Equ. 1 using Farnebäck optical flow [47] to compute pixel-wise displacement vectors and capture inter-frame myocardial motion,

$$\mathbf{F}^{(t)} = \Psi_{\text{FB}}(\mathcal{I}_t, \mathcal{I}_{t+1}), \quad (1)$$

where $\mathbf{F}^{(t)}$ represents the computed motion vector field between consecutive frames \mathcal{I}_t and \mathcal{I}_{t+1} , with Ψ_{FB} denoting the optical flow operator.

The global region-of-interest was centered on ventricular motion trajectories, with a standardized 96-pixel window centered on the cardiac chambers. This approach selectively enhances visualization of biventricular

wall motion while eliminating confounding signals from extracardiac structures, enabling precise quantification of regional contractility abnormalities without manual segmentation.

4.4 Stage I: motion-aware multi-view distillation

The PRISM’s knowledge distillation framework gains insights from the DINOv2 [48] paradigm in natural image processing, adapting its self-supervised principles to multi-view cardiac imaging through asymmetrical processing pathways.

The teacher pathway integrates long-axis views comprising 2-chamber, 3-chamber and 4-chamber orientations, capturing comprehensive myocardial dynamics across multiple anatomical planes. Simultaneously, the student pathway analyzes spatially compressed short-axis sequences through dimensionality-reduced representations, learning condensed motion features from the cine SA data. Feature alignment between pathways is achieved via a distillation optimization expressed in Equ. 2,

$$\mathcal{L}_{\text{Stage I}} = \tau^2 D_{\text{KL}} \left(p^{(s)} \| \bar{p}^{(t)} \right) + \lambda \mathcal{L}_{\text{contrastive}}, \quad (2)$$

where the teacher’s multi-view feature embeddings, specifically denoted as $\bar{p}^{(t)}$, guide the student’s SA-derived representations $p^{(s)}$ through Kullback-Leibler divergence [49] minimization. This mechanism transfers knowledge regarding cross-view myocardial motion patterns to the compressed SA pathway. The complementary contrastive component, identified as $\mathcal{L}_{\text{contrastive}}$ and instantiated via an InfoNCE-based formulation [50], coordinates phase-specific feature consistency within individual patients while simultaneously differentiating motion characteristics across distinct subjects. This dual pathway strategy yields spatiotemporally coherent motion tokens encoding prognostic signatures characteristic of ventricular dysfunction.

4.5 Stage II: EHR-attention directive

Given a medical prompt $\mathcal{T} \in \mathbb{V}^L$, where \mathbb{V} denotes the clinical vocabulary and L the sequence length, the routing module \mathcal{R} generates a sparse group attention vector $\alpha = [\alpha_1, \dots, \alpha_G]$ through semantic parsing expressed in Equ. 3,

$$\alpha = \mathcal{R}(\text{Embed}(\mathcal{T})), \quad (3)$$

where each α_i is approximately 0, 0.5, or 1.

The architecture then branches into three parallel processing streams to establish cross-modal alignment.

The *Cross-Attention Fusion* component computes query projections $\mathbf{Q} = \mathbf{P}\mathbf{W}_Q \in \mathbb{R}^{N_P \times d_{\text{attn}}}$ from BERT-encoded [51] prompt embeddings $\mathbf{P} \in \mathbb{R}^{N_P \times d_P}$, while spatial-temporal visual features $\mathbf{Z}^{(s)} \in \mathbb{R}^{N_I \times d_I}$ generate keys and values via linear projection $\mathbf{K} = \mathbf{V} = \mathbf{Z}^{(s)}\mathbf{W}_K$. The aligned image representation emerges through multi-head attention followed by dimension compression in Equ. 4,

$$\mathbf{Z}_{\text{align}} = \text{LayerNorm} \left(\mathbf{W}_p \cdot \mathbb{E}_l [\mathbf{Q}_l \oplus \text{Attn}(\mathbf{Q}_l, \mathbf{K}, \mathbf{V})] \right), \quad (4)$$

where \oplus denotes concatenation along the sequence dimension and $\mathbb{E}_l[\cdot]$ implements average pooling over the prompt token axis. \mathbf{Q}_l is a prompt query constructed in an inference-intuitive manner based on given medical prompt.

For EHR feature processing, the *Embedding Engine* converts categorical EHR variables $\mathbf{e} \in \mathbb{Z}^m$ into group-specific representations. Each feature e_f in group g is embedded through dedicated layers $\phi_f(\cdot)$, then aggregated with routing weights α_g demonstrated in Equ. 5,

$$\mathbf{Z}_{\text{ehr}}^g = \alpha_g \cdot \mathbb{E}_{f \in S_g} [\phi_f(e_f)], \quad \mathbf{Z}_{\text{ehr}} = \sum_{g=1}^G \mathbf{Z}_{\text{ehr}}^g, \quad (5)$$

where S_g indexes clinical feature subgroups. Finally, the *Visual Anchor* stream preserves original feature topology through detached projection of spatial-temporal features outlined in Equ. 6,

$$\mathbf{Z}_{\text{ref}} = \text{LayerNorm} \left(\mathbf{W}_r \cdot \mathbb{E}[\mathbf{Z}^{(s)}] \right). \quad (6)$$

4.6 Alignment Objectives

The dual-objective loss enforces both semantic alignment and structural preservation. The EHR-Consistent Triangulation Loss operates on valid triplets (i, j, k) satisfying $\text{sim}_{EHR}(\mathbf{e}^i, \mathbf{e}^j) > \text{sim}_{EHR}(\mathbf{e}^i, \mathbf{e}^k) + \delta$ as defined in Equ. 7,

$$\mathcal{L}_{tri} = \sum_{\mathcal{T}} \max \left(0, \|\mathbf{Z}_{align}^i - \mathbf{Z}_{ehr}^j\|_2^2 - \|\mathbf{Z}_{align}^i - \mathbf{Z}_{ehr}^k\|_2^2 + \delta \right), \quad (7)$$

with margin $\delta = 0.2$. The Topology Preservation Loss combining geometric constraints is calculated in Equ. 8,

$$\mathcal{L}_{pres} = \frac{1}{B} \sum_{i=1}^B \|\mathbf{Z}_{align}^i - \mathbf{Z}_{ref}\|_2^2, \quad (8)$$

where \mathcal{D}_{SW} denotes sliced Wasserstein distance. Then we obtain the composite objective in Equ. 9,

$$\mathcal{L}_{total} = \mathcal{L}_{tri} + \beta \mathcal{L}_{pres}. \quad (9)$$

4.7 Stage III: survival prediction

Clinical indicators $\mathbf{e} \in \mathbb{R}^{d_m}$ derived from tabulated EHR provide essential information for constructing a multimodal fusion module together with pre-trained image tokens $\mathbf{r} = \mathbb{E}(Q_{img}) \in \mathbb{R}^{d_c}$. These features are concatenated to form the combined vector $\mathbf{x}_{fused} = \text{concat}[\mathbf{e}, \mathbf{r}] \in \mathbb{R}^{d_m+d_c}$, integrating informative data from both clinical and imaging domains.

A standard CoxPH head is applied, where the coefficients β_k serve to automatically weight the contributions of each fused feature. The hazard function is modeled in Equ. 10,

$$h(t|\mathbf{x}_{fused}) = h_0(t) \exp \left(\sum_k \beta_k x_{fused_k} \right), \quad (10)$$

with $h_0(t)$ representing the baseline hazard function.

The training objective minimizes the negative log-partial likelihood given by Equ. 11,

$$\mathcal{L}_{Cox} = - \sum_{i:\delta_i=1} \left[\theta^\top \mathbf{x}_{fused}^{(i)} - \log \sum_{j \in R(t_i)} \exp \left(\theta^\top \mathbf{x}_{fused}^{(j)} \right) \right] + \lambda \|\theta\|_2^2, \quad (11)$$

where $\theta = [\beta_1, \dots, \beta_m]^\top$ denotes the vector of regression parameters, δ_i indicates whether the event occurred for subject i , and $R(t_i)$ corresponds to the risk set at survival time t_i .

4.8 Evaluation metrics

In this study, we utilized C-index [52] and AUC as primary evaluation metrics. The C-index assesses the discriminatory power of the model by measuring the proportion of all comparable subject pairs whose predicted risks are correctly ordered relative to their observed survival times. Formally, it is defined in Equ. 12,

$$\text{C-index} = \frac{\sum_{i,j} \mathbb{I}(t_i < t_j) \mathbb{I}(r_i > r_j) \delta_i}{\sum_{i,j} \mathbb{I}(t_i < t_j) \delta_i}, \quad (12)$$

where δ_i indicates the occurrence of the event of interest, and $r_i = \beta^\top \mathbf{x}_{fused}^i$ represents the risk score derived from the prognostic model. Complementarily, we incorporated AUC to quantify the model's sensitivity and specificity in stratifying patients with respect to event status across varying decision thresholds.

4.9 Implementation details

The model was implemented in the PyTorch environment and trained using NVIDIA-H100 GPUs with CUDA 12.2. Specifically, Stages I and III were conducted on a single H100 GPU, whereas Stage II utilized a 4-GPU H100 setup. The GPU-to-CPU ratio was maintained at approximately 1 to 15. Optimization was performed using the Adam optimizer [53] with an initial learning rate of 5×10^{-5} and weight decay set to 1×10^{-5} . A batch size of 16 was used throughout, and models were trained for 50 epochs with a StepLR learning rate scheduler. The 4D cardiac cine MRI inputs were uniformly resized to dimensions of $24 \times 24 \times 96 \times 96$, indicating depth, temporal frames, height, and width. A total of 41 EHR features were incorporated, with 579, 672, 406, and 313 samples included from GLCCM, AZCCM, RJCCM, and TJCCM, respectively.

Standard data partitioning schemes were employed, with a training-to-validation ratio of 7:3 for self-supervised learning during Stages I and II, and a split of 6:2:2 for training, validation, and testing sets in the survival prediction stage (Stage III). In Stage II, each image sample was paired with 50 unique medical prompt variants. During Stage III, grid search combined with stratified sampling was used for hyperparameter tuning, and feature selection was performed using stepwise regression and Lasso regularization within the CoxPH. The IECV setting is implemented by fixing the same test set within each cohort. For internal validation, training and testing are performed on the individual cohort separately. For external validation, the model is trained on the combined training sets of the remaining cohorts and tested on the same test set as used in the internal validation.

Declarations

Ethics approval

The Institutional Review Boards (IRBs) of all participating centers approved this research. To protect patient privacy, informed consent was waived by the IRBs, and all data were anonymized prior to their use in model training, testing, and reader studies.

Competing interests

The authors declare no competing interests.

Author contribution

H.S. designed the model and performed experiments. H.S. and S.R. developed and provided survival analysis code. H.S., S.R., and Y.G. processed the experimental data and documented control experiment details. J.X., X.C., T.Y., and L.W. provided cine imaging data, medical diagnoses, and electronic health records. L.W. and X.W. supervised the research direction. H.S. drafted the manuscript. J.X., L.W., and X.W. contributed to manuscript editing and revision.

Acknowledgements

This work was supported by the Shanghai Artificial Intelligence Laboratory, the National Program for Support of Top-notch Young Professionals from the Organization Department of the Central Committee of the Communist Party of China, the National Natural Science Foundation of China (No.82171884, No. 82471931), the Shanghai Municipal Commission of Science and Technology Medical Innovation Research Special Project (23Y11906900), and the Shanghai Municipal Health Commission Outstanding Youth Grant.

References

- [1] Frank L. J. Visseren, François Mach, Yvo M. Smulders, David Carballo, Konstantinos C. Koskinas, Magnus Bäck, Athanase Benetos, Alessandro Biffi, José Manuel Boavida, Davide Capodanno, Bernard Cosyns, Charlotte Crawford, Constantinos H. Davos, Isabelle Desormais, Emanuele Di Angelantonio, Oscar H. Franco, Sigrun Halvorsen, F. D. Richard Hobbs, Monique Hollander, Ewa A. Jankowska, Matthias Michal, Simona Sacco, Naveed Sattar, Lale Tokgozoglu, Serena Tonstad, Kostas P. Tsioufis,

- Ineke van Dis, Isabelle C. van Gelder, Christoph Wanner, Bryan Williams, ESC National Cardiac Societies, and ESC Scientific Document Group. 2021 esc guidelines on cardiovascular disease prevention in clinical practice. *European Heart Journal*, 42(34):3227–3337, 2021. Erratum in: *Eur Heart J*. 2022 Nov 7;43(42):4468.
- [2] Seth S. Martin, Abigail W. Aday, Zainab I. Almarzooq, Cheryl A. M. Anderson, Pankaj Arora, Christy L. Avery, Christine M. Baker-Smith, Barbie Barone Gibbs, Alexandra Z. Beaton, Amelia K. Boehme, Yvonne Commodore-Mensah, Mary E. Currie, Mitchell S. V. Elkind, Kelly R. Evenson, Giselle Generoso, Dwayne G. Heard, Swapnil Hiremath, Mary C. Johansen, Ramin Kalani, Dhruv S. Kazi, David Ko, Jun Liu, Jared W. Magnani, Erin D. Michos, Michael E. Mussolino, Sankar D. Navaneethan, Neha I. Parikh, Sarah M. Perman, Ranjan Poudel, Mary Rezk-Hanna, Gregory A. Roth, Norrina B. Shah, Marie-Pierre St-Onge, Erin L. Thacker, Connie W. Tsao, Stephen M. Urbut, Harriette G. C. Van Spall, Jenifer H. Voeks, Nicole Y. Wang, Nathan D. Wong, Susan S. Wong, Kristine Yaffe, Latha P. Palaniappan, American Heart Association Council on Epidemiology, Prevention Statistics Committee, and Stroke Statistics Subcommittee. 2024 heart disease and stroke statistics: A report of us and global data from the american heart association. *Circulation*, 149(8):e347–e913, 2024. Erratum in: *Circulation*. 2024 May 7;149(19):e1164.
 - [3] Luis F. Reyes, Eduardo Garcia-Gallo, Srinivas Murthy, Yuliana V. Fuentes, Carlos C. Serrano, Estefanía D. Ibáñez-Prada, Jinsook Lee, Amanda Rojek, Benjamin W. Citarella, Bruno P. Gonçalves, Jake Dunning, Indrek Rätsep, Alejandro E. Viñan-Garces, Christiana Kartsonaki, Jordi Rello, Ignacio Martin-Loeches, Manu Shankar-Hari, Piero L. Olliaro, Laura Merson, and ISARIC Characterisation Group. Major adverse cardiovascular events (mace) in patients with severe covid-19 registered in the isaric who clinical characterization protocol: A prospective, multinational, observational study. *Journal of Critical Care*, 77:154318, 2023.
 - [4] Zhiyuan Xu, Xiao Xu, Xuemei Zhu, Kai Niu, Jie Dong, and Zhiqiang He. Attention-based deep learning model for prediction of major adverse cardiovascular events in peritoneal dialysis patients. *IEEE Journal of Biomedical and Health Informatics*, 28(2):1101–1109, 2024.
 - [5] Elliott Bosco, Leon Hsueh, Kevin W. McConeghy, Stefan Gravenstein, and Elie Saade. Major adverse cardiovascular event definitions used in observational analysis of administrative databases: a systematic review. *BMC Medical Research Methodology*, 21, 2021.
 - [6] Aryabod Razipour, Kajetan Grodecki, Nipun Manral, Jolien Geers, Heidi Gransar, Aakash Shanbhag, Robert J.H. Miller, Alan Rozanski, Daniel S. Berman, Piotr J. Slomka, and Damini Dey. Ai-derived automated quantification of cardiac chambers and myocardium from non-contrast ct: Prediction of major adverse cardiovascular events in asymptomatic subjects. *Atherosclerosis*, 401:119098, 2025.
 - [7] M. Schrempf, D. Kramer, S. Jauk, S. P. K. Veeranki, W. Leodolter, and P. P. Rainer. Machine learning based risk prediction for major adverse cardiovascular events. In *Studies in Health Technology and Informatics*, volume 279, pages 136–143, 2021.
 - [8] Jialu Pi, Juan Maria Farina, Rimita Lahiri, Jiwoong Jeong, Archana Gurudu, Hyung-Bok Park, Chieh-Ju Chao, Chadi Ayoub, Reza Arsanjani, and Imon Banerjee. Moscard – causal reasoning and deconfounding for multimodal opportunistic screening of cardiovascular adverse events, 2025.
 - [9] Shaohao Rui, Haoyang Su, Jinyi Xiang, Lian-Ming Wu, and Xiaosong Wang. Cardiocot: Hierarchical reasoning for multimodal survival analysis, 2025.
 - [10] Tao Hu, Joshua Freeze, Prerna Singh, Justin Kim, Yingnan Song, Hao Wu, Juhwan Lee, Sadeer Al-Kindi, Sanjay Rajagopalan, David L. Wilson, and Ammar Hoori. Ai prediction of cardiovascular events using opportunistic epicardial adipose tissue assessments from ct calcium score, 2024.
 - [11] Yingnan Song, Hao Wu, Juhwan Lee, Justin Kim, Ammar Hoori, Tao Hu, Vladislav Zimin, Mohamed Makhoulouf, Sadeer Al-Kindi, Sanjay Rajagopalan, Chun-Ho Yun, Chung-Lieh Hung, and David L. Wilson. Pericoronary adipose tissue feature analysis in ct calcium score images with comparison to coronary cta, 2024.

- [12] Rohan Dhamdhere, Gourav Modanwal, Mohamed H. E. Makhoul, Neda Shafiabadi Hassani, Satvika Bharadwaj, Pingfu Fu, Ioannis Milioglou, Mahboob Rahman, Sadeer Al-Kindi, and Anant Madabhushi. Star-echo: A novel biomarker for prognosis of mace in chronic kidney disease patients using spatiotemporal analysis and transformer-based radiomics models. In Hayit Greenspan, Anant Madabhushi, Parvin Mousavi, Septimiu Salcudean, James Duncan, Tanveer Syeda-Mahmood, and Russell Taylor, editors, *Medical Image Computing and Computer Assisted Intervention – MICCAI 2023*, pages 284–294, Cham, 2023. Springer Nature Switzerland.
- [13] Amara Tariq, Oana Dumitrascu, Man Luo, Gina Dumkrieger, Todd J. Schwedt, Catherine Chong, and Imon Banerjee. Multi-modal predictive model for mace risk estimation in patients with migraine. In *2024 IEEE 12th International Conference on Healthcare Informatics (ICHI)*, pages 684–687, 2024.
- [14] Y. Kim, H. Kang, H. Seo, et al. Development and transfer learning of self-attention model for major adverse cardiovascular events prediction across hospitals. *Scientific Reports*, 14:23443, 2024.
- [15] P. Zhang, L. Wu, T. Zou, Z. Zou, J. Tu, R. Gong, and J. Kuang. Machine learning for early prediction of major adverse cardiovascular events after first percutaneous coronary intervention in patients with acute myocardial infarction: Retrospective cohort study. *JMIR Formative Research*, 8:e48487, 2024.
- [16] Chirag Nagpal, Xinyu Li, and Artur Dubrawski. Deep survival machines: Fully parametric survival regression and representation learning for censored data with competing risks. *IEEE Journal of Biomedical and Health Informatics*, 25(8):3163–3175, 2021.
- [17] Anna Meier, Katharina Nekolla, Lucy C Hewitt, Stephanie Earle, Takaki Yoshikawa, Takashi Oshima, Yo Miyagi, Ralf Huss, Gerhard Schmidt, and Heike I. Grabsch. Hypothesis-free deep survival learning applied to the tumour microenvironment in gastric cancer. *Journal of Pathology: Clinical Research*, 6(4):273–282, Oct 2020.
- [18] D. R. Cox. Regression models and life-tables. *Journal of the Royal Statistical Society: Series B (Methodological)*, 34(2):187–202, 12 2018.
- [19] CI Terada, K Onoue, T Fujii, H Itami, K Morita, T Uchiyama, M Takeda, H Nakagawa, T Nakano, Y Baba, K Amemiya, Y Saito, K Hatakeyama, and C Ohbayashi. Histopathological and epigenetic changes in myocardium associated with cancer therapy-related cardiac dysfunction. *ESC Heart Failure*, 9(5):3031–3043, 2022. Epub 2022 Jun 23.
- [20] MH Udin, SS Sunder, S Nepali, S Kattel, A Abdelradi, ST Doyle, CN Ionita, Q Liu, UC Sharma, and S Pokharel. Differential cardiac impacts of hematological malignancies and solid tumors: a histopathological and biomarker study. *Cardio-Oncology*, 10(1):90, Dec 19 2024.
- [21] Hongxiao Wang, Yang Yang, Zhuo Zhao, Pengfei Gu, Nishchal Sapkota, and Danny Z. Chen. Pathgptomic: A balanced multi-modal learning framework for survival outcome prediction. In *2024 IEEE International Symposium on Biomedical Imaging (ISBI)*, pages 1–5, 2024.
- [22] Yihang Chen, Weiqin Zhao, and Lequan Yu. Transformer-based multimodal fusion for survival prediction by integrating whole slide images, clinical, and genomic data. In *2023 IEEE 20th International Symposium on Biomedical Imaging (ISBI)*, pages 1–5, 2023.
- [23] Caroline Petitjean and Jean-Nicolas Dacher. A review of segmentation methods in short axis cardiac mr images. *Medical Image Analysis*, 15(2):169–184, 2011.
- [24] Igor Klem, Jonathan W. Weinsaft, Tristram D. Bahnson, Don Hegland, Han W. Kim, Brenda Hayes, Michele A. Parker, Robert M. Judd, and Raymond J. Kim. Assessment of myocardial scarring improves risk stratification in patients evaluated for cardiac defibrillator implantation. *Journal of the American College of Cardiology*, 60(5):408–420, 2012.
- [25] M. L. Li, R. Y. Shi, J. Y. Zheng, J. Y. Xiang, W. Hedges, J. Liang, J. Hu, J. Chen, L. Zhao, and L. M. Wu. Myocardial mri cine radiomics: A novel approach to risk-stratification for major adverse cardiovascular events in patients with st-elevation myocardial infarction. *Journal of Magnetic Resonance Imaging*, 62(2):430–443, 2025.

- [26] R. E. Konst, M. Parker, L. Bhatti, Y. Kaolawanich, F. Alenezi, S. E. Elias-Smale, R. Nijveldt, and R. J. Kim. Prognostic value of cardiac magnetic resonance imaging in patients with a working diagnosis of minoca—an outcome study with up to 10 years of follow-up. *Circulation: Cardiovascular Imaging*, 16(8):e014454, 2023.
- [27] Shingo Kato, Kei Fukui, Shohei Kodama, and et al. Prognostic value of resting coronary sinus flow determined by phase-contrast cine cardiovascular magnetic resonance in patients with known or suspected coronary artery disease. *Journal of Cardiovascular Magnetic Resonance*, 23(1):97, 2021.
- [28] Tony Xu, Sepehr Hosseini, Chris Anderson, Anthony Rinaldi, Rahul G. Krishnan, Anne L. Martel, and Maged Goubran. A generalizable 3d framework and model for self-supervised learning in medical imaging, 2025.
- [29] Lei Zhou, Huidong Liu, Joseph Bae, Junjun He, Dimitris Samaras, and Prateek Prasanna. Self pre-training with masked autoencoders for medical image classification and segmentation, 2023.
- [30] Hong-Yu Zhou, Chixiang Lu, Sibe Yang, Xiaoguang Han, and Yizhou Yu. Preservational learning improves self-supervised medical image models by reconstructing diverse contexts, 2022.
- [31] Marc C. Williams, Bartosz P. Bednarski, Krzysztof Pieszko, et al. Unsupervised learning to characterize patients with known coronary artery disease undergoing myocardial perfusion imaging. *European Journal of Nuclear Medicine and Molecular Imaging*, 50:2656–2668, 2023.
- [32] Haoyang Su, Shaohao Rui, Jinyi Xiang, Lianming Wu, and Xiaosong Wang. Ctsl: Codebook-based temporal-spatial learning for accurate non-contrast cardiac risk prediction using cine mris, 2025.
- [33] Ewout W. Steyerberg and Frank E. Harrell. Prediction models need appropriate internal, internal-external, and external validation. *Journal of Clinical Epidemiology*, 69:245–247, 2016.
- [34] A.W.F. Edwards. Chapter 67 - r.a. fischer, statistical methods for research workers, first edition (1925). In I. Grattan-Guinness, Roger Cooke, Leo Corry, Pierre Crépel, and Niccolo Guicciardini, editors, *Landmark Writings in Western Mathematics 1640-1940*, pages 856–870. Elsevier Science, Amsterdam, 2005.
- [35] E. L. Kaplan and Paul Meier. *Nonparametric Estimation from Incomplete Observations*, pages 319–337. Springer New York, New York, NY, 1992.
- [36] American Heart Association Writing Group on Myocardial Segmentation, Registration for Cardiac Imaging; Manuel D. Cerqueira, Neil J. Weissman, Vasken Dilsizian, Alice K. Jacobs, Sanjiv Kaul, Warren K. Laskey, Dudley J. Pennell, John A. Rumberger, Thomas Ryan, and Mario S. Verani. Standardized myocardial segmentation and nomenclature for tomographic imaging of the heart. *Circulation*, 105(4):539–542, 2002.
- [37] Murray Rosenblatt. Remarks on Some Nonparametric Estimates of a Density Function. *The Annals of Mathematical Statistics*, 27(3):832 – 837, 1956.
- [38] Tatiana Kuznetsova, Jan Bogaert, Malgorzata Kloch-Badelek, Diederick Thijs, Lutgarde Thijs, and Jan A Staessen. Association of left ventricular diastolic function with systolic dyssynchrony: a population study. *Eur Heart J Cardiovasc Imaging*, 14(5):471–479, May 2013. Epub 2012 Sep 21.
- [39] LJ Daniels, C Macindoe, P Koutsifeli, M Annandale, SL James, LE Watson, S Coffey, AJA Raaijmakers, KL Weeks, JR Bell, JV Janssens, CL Curl, LMD Delbridge, and KM Mellor. Myocardial deformation imaging by 2d speckle tracking echocardiography for assessment of diastolic dysfunction in murine cardiopathology. *Scientific Reports*, 13(1):12344, 2023.
- [40] M. J. Warner and V. S. Tivakaran. Inferior myocardial infarction, Feb 12 2023. In: StatPearls [Internet]. Treasure Island (FL): StatPearls Publishing; 2025 Jan–. PMID: 29262146.
- [41] DeepSeek-AI, Daya Guo, Dejian Yang, Haowei Zhang, Junxiao Song, Ruoyu Zhang, Runxin Xu, Qihao Zhu, Shirong Ma, Peiyi Wang, Xiao Bi, Xiaokang Zhang, Xingkai Yu, Yu Wu, Z. F. Wu, Zhibin Gou, Zhihong Shao, Zhuoshu Li, Ziyi Gao, Aixin Liu, Bing Xue, Bingxuan Wang, Bochao Wu, Bei Feng,

- Chengda Lu, Chenggang Zhao, Chengqi Deng, Chenyu Zhang, Chong Ruan, Damai Dai, Deli Chen, Dongjie Ji, Erhang Li, Fangyun Lin, Fucong Dai, Fuli Luo, Guangbo Hao, Guanting Chen, Guowei Li, H. Zhang, Han Bao, Hanwei Xu, Haocheng Wang, Honghui Ding, Huajian Xin, Huazuo Gao, Hui Qu, Hui Li, Jianzhong Guo, Jiashi Li, Jiawei Wang, Jingchang Chen, Jingyang Yuan, Junjie Qiu, Junlong Li, J. L. Cai, Jiaqi Ni, Jian Liang, Jin Chen, Kai Dong, Kai Hu, Kaige Gao, Kang Guan, Kexin Huang, Kuai Yu, Lean Wang, Lecong Zhang, Liang Zhao, Litong Wang, Liyue Zhang, Lei Xu, Leyi Xia, Mingchuan Zhang, Minghua Zhang, Minghui Tang, Meng Li, Miaojun Wang, Mingming Li, Ning Tian, Panpan Huang, Peng Zhang, Qiancheng Wang, Qinyu Chen, Qiushi Du, Ruiqi Ge, Ruisong Zhang, Ruizhe Pan, Runji Wang, R. J. Chen, R. L. Jin, Ruyi Chen, Shanghao Lu, Shangyan Zhou, Shanhuang Chen, Shengfeng Ye, Shiyu Wang, Shuiping Yu, Shunfeng Zhou, Shuting Pan, S. S. Li, Shuang Zhou, Shaoqing Wu, Shengfeng Ye, Tao Yun, Tian Pei, Tianyu Sun, T. Wang, Wangding Zeng, Wanbiao Zhao, Wen Liu, Wenfeng Liang, Wenjun Gao, Wenqin Yu, Wentao Zhang, W. L. Xiao, Wei An, Xiaodong Liu, Xiaohan Wang, Xiaokang Chen, Xiaotao Nie, Xin Cheng, Xin Liu, Xin Xie, Xingchao Liu, Xinyu Yang, Xinyuan Li, Xuecheng Su, Xuheng Lin, X. Q. Li, Xiangyue Jin, Xiaojin Shen, Xiaosha Chen, Xiaowen Sun, Xiaoxiang Wang, Xinnan Song, Xinyi Zhou, Xianzu Wang, Xinxia Shan, Y. K. Li, Y. Q. Wang, Y. X. Wei, Yang Zhang, Yanhong Xu, Yao Li, Yao Zhao, Yaofeng Sun, Yaohui Wang, Yi Yu, Yichao Zhang, Yifan Shi, Yiliang Xiong, Ying He, Yishi Piao, Yisong Wang, Yixuan Tan, Yiyang Ma, Yiyuan Liu, Yongqiang Guo, Yuan Ou, Yudian Wang, Yue Gong, Yuheng Zou, Yujia He, Yunfan Xiong, Yuxiang Luo, Yuxiang You, Yuxuan Liu, Yuyang Zhou, Y. X. Zhu, Yanhong Xu, Yanping Huang, Yaohui Li, Yi Zheng, Yuchen Zhu, Yunxian Ma, Ying Tang, Yukun Zha, Yuting Yan, Z. Z. Ren, Zehui Ren, Zhangli Sha, Zhe Fu, Zhean Xu, Zhenda Xie, Zhengyan Zhang, Zhewen Hao, Zhicheng Ma, Zhigang Yan, Zhiyu Wu, Zihui Gu, Zijia Zhu, Zijun Liu, Zilin Li, Ziwei Xie, Ziyang Song, Zizheng Pan, Zhen Huang, Zhipeng Xu, Zhongyu Zhang, and Zhen Zhang. Deepseek-r1: Incentivizing reasoning capability in llms via reinforcement learning, 2025.
- [42] S. Chopannejad, F. Sadoughi, R. Bagherzadeh, and S. Shekarchi. Predicting major adverse cardiovascular events in acute coronary syndrome: A scoping review of machine learning approaches. *Applied Clinical Informatics*, 13(3):720–740, 2022.
- [43] Y. Zhai, H. Shang, Y. Li, N. Zhang, J. Zhang, and S. Wu. A systematic review of risk factors for major adverse cardiovascular events in patients with coronary heart disease who underwent percutaneous coronary intervention. *Frontiers in Physiology*, 16:1514585, 2025.
- [44] Alison K. Wright, Evangelos Kontopantelis, Richard Emsley, Iain Buchan, Mamas A. Mamas, Naveed Sattar, Darren M. Ashcroft, and Martin K. Rutter. Cardiovascular risk and risk factor management in type 2 diabetes mellitus. *Circulation*, 139(24):2742–2753, 2019.
- [45] Shiyi Tao, Lintong Yu, Jun Li, Li Huang, Xuanchun Huang, Wenjie Zhang, Zicong Xie, Yuqing Tan, and Deshuang Yang. Association between the triglyceride-glucose index and 1-year major adverse cardiovascular events in patients with coronary heart disease and hypertension. *Cardiovascular Diabetology*, 22(1):305, 2023.
- [46] L. Huang, J. Zhang, Q. Huang, et al. In-hospital major adverse cardiovascular events after primary percutaneous coronary intervention in patients with acute st-segment elevation myocardial infarction: a retrospective study under the china chest pain center (standard center) treatment system. *BMC Cardiovascular Disorders*, 23:198, 2023.
- [47] Gunnar Farneback. Two-frame motion estimation based on polynomial expansion. In Josef Bigun and Tomas Gustavsson, editors, *Image Analysis*, pages 363–370, Berlin, Heidelberg, 2003. Springer Berlin Heidelberg.
- [48] Maxime Oquab, Timothée Darcet, Théo Moutakanni, Huy Vo, Marc Szafraniec, Vasil Khalidov, Pierre Fernandez, Daniel Haziza, Francisco Massa, Alaaeldin El-Nouby, Mahmoud Assran, Nicolas Ballas, Wojciech Galuba, Russell Howes, Po-Yao Huang, Shang-Wen Li, Ishan Misra, Michael Rabbat, Vasu Sharma, Gabriel Synnaeve, Hu Xu, Hervé Jegou, Julien Mairal, Patrick Labatut, Armand Joulin, and Piotr Bojanowski. Dinov2: Learning robust visual features without supervision, 2024.
- [49] Solomon Kullback and R. A. Leibler. On information and sufficiency. *Annals of Mathematical Statistics*, 22:79–86, 1951.

- [50] Ting Chen, Simon Kornblith, Mohammad Norouzi, and Geoffrey Hinton. A simple framework for contrastive learning of visual representations. *arXiv preprint arXiv:2002.05709*, 2020.
- [51] Mikhail Koroteev. Bert: A review of applications in natural language processing and understanding, 03 2021.
- [52] Jr. Frank E. Harrell. Regression modeling strategies: With applications to linear models, logistic regression, and survival analysis. 2001.
- [53] Diederik P. Kingma and Jimmy Ba. Adam: A method for stochastic optimization. *CoRR*, abs/1412.6980, 2014.